Negatively-curved warped nanographene self-assembled on metal surfaces

José I. Urgel,[‡,] Marco Di Giovannantonio,[‡] Yasutomo Segawa,[#,ϕ] Pascal Ruffieux,[‡] Lawrence T. Scott,[†] Carlo A. Pignedoli,[‡] Kenichiro Itami,[#,ϕ,§,]* and Roman Fasel [‡,∥,]**

[‡] Empa, Swiss Federal Laboratories for Materials Science and Technology, 8600 Dübendorf, Switzerland

[†] Merkert Chemistry Center, Boston College Chestnut Hill, MA 02467-3860 (USA)

[#] Graduate School of Science, [ϕ]JST, ERATO, Itami Molecular Nanocarbon Project, and [§]Institute of Transformative Bio-Molecules (WPI-ITbM), Nagoya University, Nagoya 464-8602, Japan

[∥] Department of Chemistry and Biochemistry, University of Bern, 3012 Bern, Switzerland

ABSTRACT

We report the investigation of a conjugated polycyclic hydrocarbon containing multiple non-benzenoid rings and exhibiting negative curvature - the warped nanographene $C_{80}H_{30}$ - adsorbed on several noble metal surfaces in an ultrahigh vacuum environment. From a detailed analysis of the molecular self-assembly at different molecular coverages *via* scanning tunneling microscopy and spectroscopy measurements in combination with theoretical modeling, the nature of the intermolecular interactions is unraveled. For high molecular coverages on Cu(111), the formation of homochiral porous networks is observed, which is rationalized by *(i)* intermolecular π-π interactions between neighboring $C_{80}H_{30}$ molecules that promotes the formation of molecular dimers, and *(ii)* enantioselective intermolecular CH···π interactions between the dimers. Such interactions are also observed after deposition of $C_{80}H_{30}$ molecules on Au(111) and Ag(111) substrates. Our results provide perspectives for the on-surface study of negatively-curved nanographenes which give prospects for the design of novel and functional chiral structures with potential use in the field of organic optoelectronics.

INTRODUCTION

In the last decades, nanometer-sized carbon materials made solely of sp^2-hybridized carbon atoms oriented in particular geometric patterns, namely nanocarbons, have changed the landscape of carbon-based nanomaterials, opening doors to new technologies due to their interesting optical, magnetic and electronic properties.[1–6] They can be classified according to their dimensionality, where fullerenes[7] (0D), carbon nanotubes[8] and graphene nanoribbons[9] (CNTs and GNRs, 1D), graphene[1] (2D) and Mackay crystals[10] (3D) are the most recognized nanocarbons, triggering tremendous interest in both scientific and technological communities. In the early 90's Mackay crystals composed of 6- and 8- or 6- and 7-membered rings, together with various other exotic nanocarbons with negative curvatures (double-concave nanostructures) were proposed for the first time.[10–13] However, despite the relevance of negative curvature in exotic nanocarbon structures,[11] nanographenes incorporating 7- or 8-membered rings comprise an ambitious challenge for organic chemists due to their relatively high ring strain. Therefore, negatively-curved nanographenes remain a relatively unexplored group of materials and only a limited number of examples of these elusive compounds currently exist.[14–18] The synthesis of a grossly-warped nanographene ($C_{80}H_{30}$),[19] which consists of five 7-membered rings and one 5-membered ring embedded in a hexagonal lattice of trigonal carbon atoms, has only recently been reported. The unique structure of the $C_{80}H_{30}$ molecule, where the presence of multiple odd-membered rings leads to a non-trivial double-concave structure, enhances characteristic properties which arise mainly from its nonplanar structure compared to planar analogues of similar size.[19] Interesting properties and potential applications of this warped nanographene have been investigated in recent studies.[19–23] For instance, it presents reversible reduction and oxidation behavior *via* charged intermediates suggesting that odd-membered ring defects in graphene can trap charges. Furthermore, $C_{80}H_{30}$ has optical and electronic properties that differ from other all-carbon families and could have potential applications for future optoelectronic devices.

In this context, complementary surface-science techniques can provide an appealing playground for the investigation of negatively-curved compounds. In particular, the use of advanced scanning probe techniques, such as scanning tunneling microscopy (STM) serve as powerful tools for direct structural and electronic characterization of molecular species on surfaces.[24]

Additionally, atomically-smooth noble metal surfaces under ultrahigh vacuum (UHV) conditions provide ideal templates for the study of intermolecular interactions, where, in many cases, the 2D confinement on a surface leads to a strong expression of chirality.[25] Planar polycyclic aromatic hydrocarbons (PAHs) such as acenes,[26–30] coronene[31–33] or pyrenes[34,35] among others, and nonplanar ball- or bowl-shaped PAHs like fullerenes and buckybowls (fragments of fullerenes)[36–40] have been extensively investigated on metallic single crystal surfaces, insulating films, or at the liquid-solid interface. However, surface studies of negatively-curved compounds have not yet been reported (see Scheme 1 for several examples of planar, curved and negatively curved PAHs).

In this article, we present a combined STM and density functional theory (DFT) study of the negatively-curved warped $C_{80}H_{30}$ molecule which is, to the best of our knowledge, the largest PAH besides fullerenes that has been investigated on metal substrates under UHV conditions. The study of a negatively-curved nanographene on surfaces provides experimental insights into the structural and electronic properties of such compounds in contact with a metallic support. Our molecular-level investigations describe a self-assembly process depending on the molecular coverage upon adsorption on several metal surfaces. At high molecular coverages, the highly nonplanar conformation of $C_{80}H_{30}$ molecules gives rise to self-assembled enantiomorphic porous networks composed of homochiral molecules and irregular supramolecular assemblies on Cu(111) and Au(111) respectively, which are stabilized by two interaction motifs attributed to π-π and CH···π interactions. For low molecular coverages, the formation of self-assembled dimers due to intermolecular π-π interactions is observed, while for medium molecular coverages the appearance of a three-fold interaction motif between adjacent dimers induced by intermolecular CH···π interactions prevails.

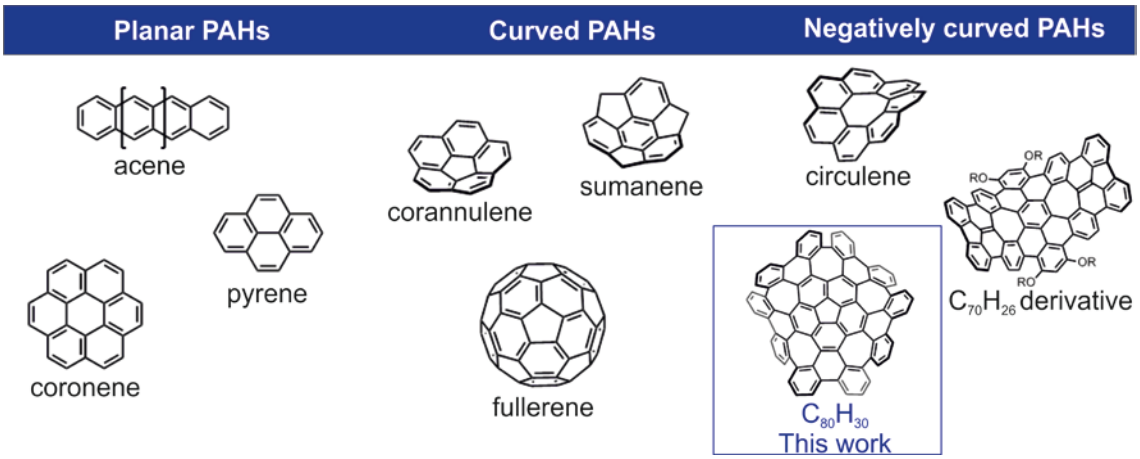

Scheme 1. Some representative examples of planar, curved and negatively curved PAHs.

RESULTS AND DISCUSSION

The synthetic route to obtain the $C_{80}H_{30}$ molecule is detailed in previous reports.[19] First, high submonolayer coverages (> 0.65 ML; ML = monolayer) of $C_{80}H_{30}$ were sublimed under UHV conditions onto an atomically-clean Cu(111) surface held at room temperature. Large scale STM images acquired at ~5 K reveal the formation of extended self-assembled supramolecular porous networks which coexist with irregular assemblies (Figure 1a). Figure 1b-d presents a detailed analysis of the STM data. It is seen that each $C_{80}H_{30}$ molecule within the networks interacts with three adjacent molecules, being stabilized by two different interaction motifs, *i.e.* motif 1 and motif 2 in Figure 1d, with an intersection angle between the hexagonal arms of $\alpha = 120°$. Such networks exhibit an inter-pore distance of 4.6 nm and an inner area of the nanopore of ~ 6.5 nm^2, whereas the unit cell vectors of the network form an angle of ~12° with respect to the close-packed directions of the Cu(111) substrate. It is worthwhile to mention that these hexagonal networks exhibit enantiomorphism with both enantiomorphic domains observed on the surface (Figure 1a). The formation of enantiomorphic domains – which are in fact also homochiral as we will show later - seems to be driven by the interaction motif 2 (see Figure S1). We note that similar coverages (> 0.5 ML) of $C_{80}H_{30}$ on Au(111) do not give rise to the formation of regular self-assembled networks based on the motifs described above (Figure S2), which is tentatively attributed to the mismatch between the molecular network and the underlying surface, together with the presence of specific nucleation sites, *i.e.* elbows of the Au(111) herringbone reconstruction.[41]

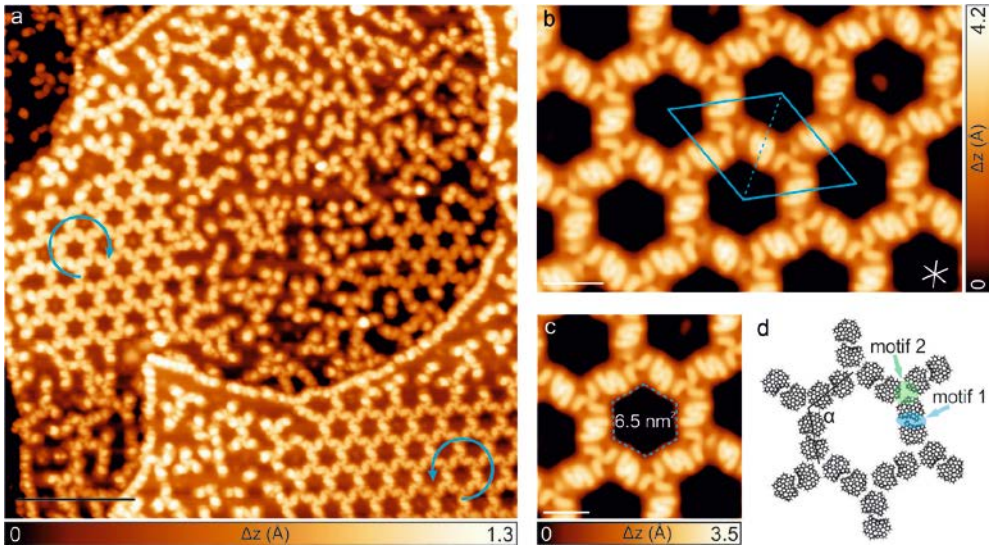

Figure 1. Formation of $C_{80}H_{30}$ self-assembled enantiomorphic hexagonal networks on Cu(111) at coverages beyond 0.65 ML. (a) Large-scale STM image of the porous networks coexisting with irregular assemblies. The blue curved arrows indicate two enantiomorphic domains on adjacent terraces. V_b = -1.5 V, I_t = 80 pA. Scale bar: 20 nm. (b) Magnified view of one of the homochiral networks observed in panel (a). The unit cell of the network comprises six molecules and is represented by the blue rhombus, while the dashed blue line indicates the inter-pore distance of the network (4.6 nm). The white star indicates the close-packed directions of Cu(111). V_b = -0.1 V, I_t = 20 pA. Scale bars: 5 nm. (c,d) High-resolution STM image (c) and the corresponding atomistic model of twelve $C_{80}H_{30}$ dimers (d), forming a single hexagonal pore with an area of 6.5 nm^2. V_b = -0.1 V, I_t = 20 pA. Scale bar: 3 nm.

In order to obtain more information about the interaction motifs that drive the formation of the self-assembled nanostructures observed after deposition of $C_{80}H_{30}$ on Cu(111) and Au(111), a detailed analysis at several molecular coverages on the different metal substrates has been realized. Deposition of $C_{80}H_{30}$ molecules at low submonolayer coverages (> 0.1 ML) on Au(111) reveals the presence of non-planar nanostructures adsorbed on the fcc regions of the surface, coexisting with linear chains on the herringbone reconstruction lines (Figure 2). The nanostructure highlighted in Figure 2a is attributed to two self-assembled $C_{80}H_{30}$ molecules rotated by 180° with respect to each other (see Figure 2b). The high-resolution STM image shows a central motif with a large apparent height of 4.3 Å, and peripheral features of lower apparent heights of 1.7-2.3 Å (measured at a sample bias of -1.5 V). These features, which are equivalent to the motif 1 described in Figure 1, suggest that the molecules adopt a highly non-planar conformation on the surface favoring π-π interactions between adjacent molecules that are

proposed to be the driving force toward the formation of such dimers. Figure 2c shows the DFT-optimized model of the dimer, wherein the corannulene cores of both molecules exhibit a parallel alignment with the underlying surface (adsorption height of 3.4 Å), in line with the similar apparent height of the central segment of each molecule; while the benzene rings at the edge of each molecule present non-equivalent apparent heights which arise from the conformational flexibility of the $C_{80}H_{30}$ upon adsorption, with a minimum C-C distance between molecules of 3.4 Å. The simulated STM image for this geometry (Figure 2d) yields excellent correspondence to the experimental image, allowing us to discern the experimental features. Importantly, it should be noted that STM images acquired with a CO-functionalized tip[42], such as the one shown in Figure 2b, reveal that the π-π interaction driving the formation of dimers is not enantioselective (see Figure S3 for the chiral and achiral adsorption of several $C_{80}H_{30}$ molecules in different dimers). This indicates a high conformational flexibility of the surface-adsorbed $C_{80}H_{30}$ molecules and very comparable adsorption energies for the different diastereomers.

To understand the nature of the interaction between the molecules in the dimers, we computed the energy of the dimer in gas phase constrained to the adsorption geometry (E_d) and the energy of both $C_{80}H_{30}$ molecules constrained to the geometry they have in the dimer (E_a and E_b). The cohesive energy of the dimer, defined as $E_d - E_a - E_b$ is 0.72 eV for the chiral (S) and achiral (A) dimer shown in Figure 2b-d. If we consider only the van der Waals interaction we obtain again a value of 0.72 eV for the cohesive energy (the difference in cohesive energy for all the possible combination of diastereomers within the dimers, *i.e.* A-A, S-S/R-R, S-A and S-R, is negligible (~0.07 eV)), demonstrating a purely dispersive character of the interaction (see Figure S4a for the computed charge density difference, depicted for the $C_{80}H_{30}$ dimer in gas phase in order to highlight the molecule-molecule contribution to the electrostatic interaction). We note that identical π-π interactions are present after deposition of molecules on different metallic substrates such as Ag(111) and Cu(111) at low coverages, leading to the formation of $C_{80}H_{30}$ dimers (see Figure S5).

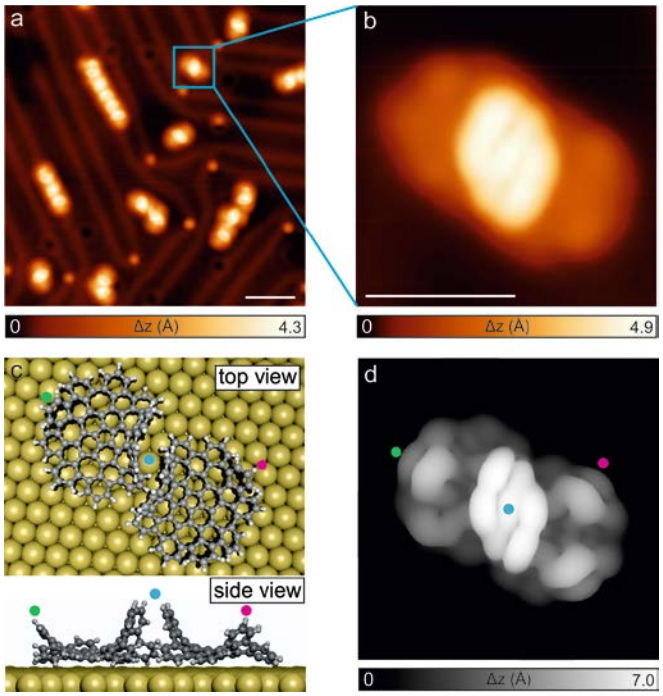

Figure 2. $C_{80}H_{30}$ dimer formation after molecular deposition on Au(111) at > 0.1 ML coverage. (a) Large-scale STM image of the surface after room temperature deposition of $C_{80}H_{30}$ molecules. V_b = 0.3 V, I_t = 30 pA. Scale bar: 5 nm. (b) High-resolution STM image of a single dimer highlighted in panel (a) acquired with a CO functionalized tip evidencing the presence of intramolecular features with several apparent heights. V_b = −1.1 V, I_t = 110 pA. Scale bar: 2 nm. (c) Top and side views of the corresponding DFT equilibrium geometry of a $C_{80}H_{30}$ dimer. (d) DFT simulated STM image of panel (c). The colored dots serve as a guide to the eye for comparing the intramolecular features in the simulated STM image and the corresponding DFT equilibrium geometry. V_b = −1.0 V.

In order to unequivocally identify and study individual $C_{80}H_{30}$ molecules, lateral manipulation experiments were performed (Figure 3a-c, manipulation parameters: V_b = -0.1 V, I_t = 5 nA). Figure 3c shows two $C_{80}H_{30}$ molecules where an achiral conformation upon adsorption on the Au(111) substrate is clearly discerned. The experimental features are well reproduced by the DFT-optimized geometry and the corresponding STM simulation of a $C_{80}H_{30}$ molecule (Figure 3d,e). Herein, one can observe the negative curvature of the molecule (a double-concave conformation) that results from the presence of a central five-membered ring at the corannulene core, together with multiple seven-membered rings that surround the corannulene, leading to two maximum apparent heights of 4.4 Å and 2.5 Å in the STM images. Such geometrical conformation is the result of van der Waals interaction between the molecule and the substrate, and differs from the lowest energy conformation adopted in the gas phase, where a maximum height of 6.3 Å has been reported.[19] DFT calculations show a deformation of the molecule from

the equilibrium gas phase geometry implying an energy loss of 0.92 eV, which is compensated by the overall adsorption energy of -3.90 eV. Remarkably, only after sublimation of the $C_{80}H_{30}$ molecules onto a highly reactive substrate such as Pt(111),[43] individual molecules are found (Figure 3f), and their adsorption geometry seems to be similar to the one obtained on the less reactive coinage metal substrates.

Next, scanning tunneling spectroscopy (STS) studies of individual molecules on Au(111) were performed. Voltage-dependent differential conductance spectra (d*I*/d*V* *vs*. V) acquired on the molecule exhibit peaks at -1.9 eV and 1.4 eV, corresponding to the positive and negative ion resonances (PIR and NIR) that derive from the highest occupied and the lowest unoccupied molecular orbitals (HOMO and LUMO), respectively. Thus, the molecule presents a large experimental electronic gap of 3.3 eV (see Figure S6), which is in good agreement with the value of 3.1 eV obtained by applying image charge corrections to the eigenvalue self-consistent GW gap calculated for the molecule adsorbed on Au(111).

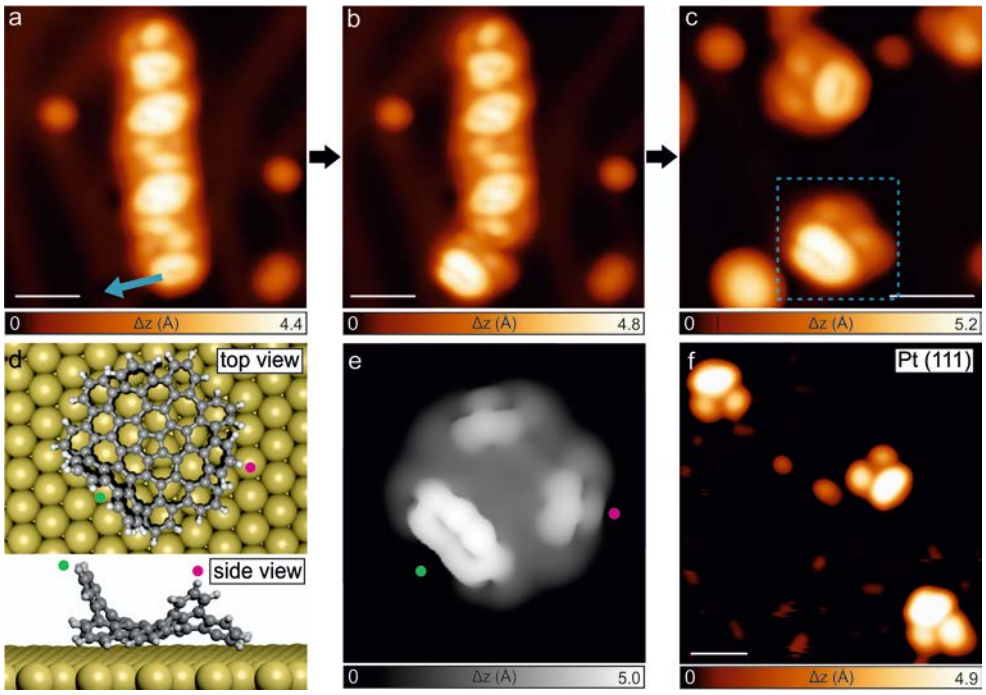

Figure 3. $C_{80}H_{30}$ identification after lateral manipulation experiments on Au (111). (a,b) High-resolution STM images of interacting $C_{80}H_{30}$ molecules before and after the lateral manipulation event. The blue arrow designates the tip trajectory (manipulation parameters: V_b = -0.1 V, I_t = 5 nA). V_b = 1.0 V, I_t = 10 pA. Scale bar: 2 nm. (c) Magnified view of same area as in (a,b) where two individual $C_{80}H_{30}$ molecules are observed after several lateral manipulation events. The blue rectangle highlights a single $C_{80}H_{30}$ molecule. V_b = 1.0 V, I_t = 20 pA. Scale bar: 2

nm. (d) Top and side views of the DFT equilibrium geometry of a $C_{80}H_{30}$ molecule. (e) DFT-simulated STM image of the molecule highlighted in panel (d). The colored dots serve as a guide to the eye for comparing the intramolecular features in the simulated STM image and the corresponding DFT equilibrium geometry. $V_b = -1.0$ V. (f) High resolution STM image of $C_{80}H_{30}$ molecules after room temperature deposition on a Pt(111) substrate. V_b = -1.0 V, I_t = 5 pA. Scale bar: 2 nm.

Higher molecular coverage of ~ 0.5 ML on Au(111) reveals the formation of a rather complex threefold motif, equivalent to the motif 2 described in Figure 1, that is not observed in the low coverage regime (Figure 4a). Ignoring a few alignment defects, the aforementioned motif is characterized by a windmill-type appearance (Figure 4b), which derives from the interaction between three $C_{80}H_{30}$ dimers. The apparent height of this threefold molecular assembly is 3.2 Å (measured at a sample bias of -1.5 V), significantly larger than the one of 2.5 Å observed for the dimers. The DFT-optimized geometry of the threefold windmill assembly (Figure 4c) together with the corresponding STM simulation (Figure 4d) allow us to discern the experimental features and to unambiguously determine the underlying structure and intermolecular interactions. In analogy to the dimer case, we computed the van der Waals contribution to the cohesive energy of a (homochiral) trimer. The total cohesive energy amounts to 0.80 eV of which 0.72 eV is due to van der Waals interactions. In this case a non-negligible electrostatic contribution of ~80 meV is present, which we attribute to CH···π bonding (see Figure S4b for the computed charge density difference, depicted for the trimer in gas phase in order to highlight the molecule-molecule contribution to the electrostatic interaction). In addition, DFT calculations show a deformation of the molecule from the equilibrium gas phase geometry implying an energy loss of 0.68 eV. The interaction motif 2 is thus driven by CH···π interactions, which arise from favorable multipole/induced multipole charge fluctuations between the tilted benzene rings of a molecule and the rim hydrogen atoms of adjacent molecules. From our DFT calculations, we find a minimum H-benzene distance of 2.55 Å.[44] Importantly, stabilization of the threefold assemblies described in Figure 4 by CH···π interactions only occurs between molecules that exhibit the same chirality. Given the conformational flexibility of the molecules, it is assumed that the molecules adapt their conformation into the one that maximizes CH···π interactions at the threefold corner point, which is the case in a homochiral situation (see Figure 4b and Figure S7 for more details). It is thus the CH···π interaction that induces homochirality in the structural windmill motif 2 and drives the formation of the enantiomorphic networks described in Figure 1.

It is well known that curved PAHs may restructure metal substrates.[45] However, any role of gold atoms in the formation of the windmill motifs can be safely excluded due to the dominant CH···π interactions, because we observe similar self-assembled motifs after deposition of $C_{80}H_{30}$ molecules onto different metal substrates such as Ag(111) or Cu(111).

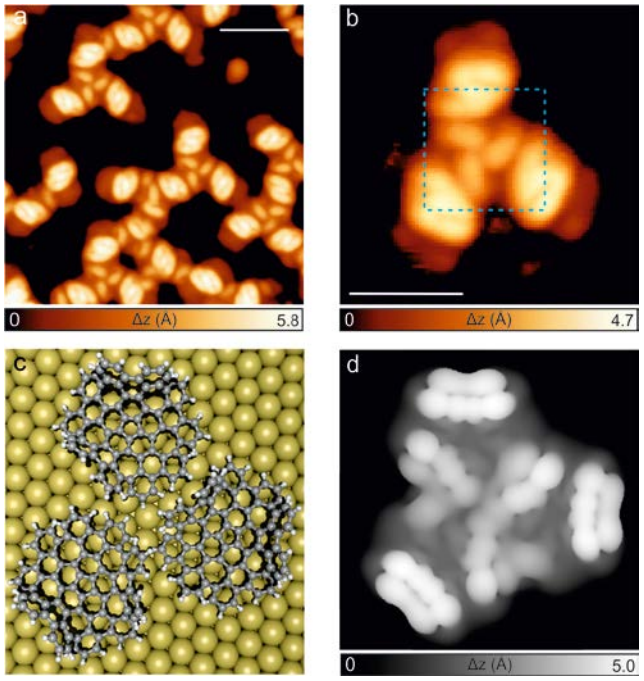

Figure 4. Formation of the windmill motif 2 driven by intermolecular C-H···π interaction after room temperature deposition of $C_{80}H_{30}$ molecules on Au(111) at coverages of ~ 0.5 ML. (a,b) High-resolution STM images of the structural windmill motif 2, revealing $C_{80}H_{30}$ trimers coexisting with individual dimers. The blue rectangle in (b) highlights the windmill motif. V_b = -0.6 V, I_t = 70 pA. Scale bars: 3 nm. (c) Top view of the corresponding DFT equilibrium geometry of the trimer highlighted in panel (b). V_b = -0.5 V. (d) DFT simulated STM image of panel (c). $V_b = -1.0$ V.

The transition from individual dimers to porous homochiral networks and to irregular assemblies on Cu(111) and Au(111), respectively, upon adsorption of the negatively-curved warped nanographene $C_{80}H_{30}$ can thus be understood as follows. For low coverages (> 0.10 ML), non-enantioselective π-π interactions (motif 1) between adjacent $C_{80}H_{30}$ molecules induce the formation of dimers on Au(111), Ag(111) and Cu(111) surfaces (Figure 2a,b and Figure S5). Medium coverages of ~ 0.50 ML promote the formation of assemblies composed of three dimers, where enantioselective CH···π interactions (motif 2) are involved (Figure 4a,b, Figure S7 and Figure S8 for trimers observed on Ag(111)). An increase in molecular coverage to more

than 0.65 ML finally leads to the formation of self-assembled homochiral networks on Cu(111) (Figure 1a-c).

CONCLUSION

In summary, we have characterized a representative member of a new family of negatively-curved nanographenes with STM at submolecular resolution upon adsorption on several metallic substrates. Depending on the noble metal substrate employed and the molecular coverage, a self-assembly process based on the nature of the intermolecular bonding, namely π-π and CH···π interactions, is achieved. The self-assembled supramolecular porous networks obtained for high molecular coverages illustrate the potential of negatively-curved nanocarbons toward the formation of regular homochiral domains, which constitutes an interesting pathway for the design of functional chiral nanostructures.

METHODS

Experiments were performed under ultrahigh vacuum conditions (base pressure below 5×10^{-10} mbar) with two Scienta-Omicron scanning probe microscopes: a low-temperature STM and a low-temperature STM/AFM.

Au(111), Ag(111), and Cu(111) single crystal surfaces were prepared by iterated cycles of sputtering with Ar^+ ions (E = 1 keV) and subsequent annealing to 750 K for 15 minutes. Clean Pt (111) single crystal surfaces were prepared through repeated cycles of Ar^+ bombardment and annealing at up to 1000 K for 15 min. All STM images shown were taken in constant current mode with electrochemically etched tungsten tips at a sample temperature of 5 K. Scanning parameters are specified in each figure caption. The $C_{80}H_{30}$ molecule was thermally deposited onto the clean Au(111) surface held at room temperature with a typical deposition rate of 0.4 Å min^{-1} (sublimation temperature ~ 710 K). The STM images were analyzed using WSxM.[46]

To obtain the equilibrium adsorption geometries within DFT, and to simulate STM, we used the CP2K code (see SI for full details). The surface/adsorbate systems were modeled within the repeated slab scheme, *i.e.*, a simulation cell contained 4 atomic layers of Au along the [111] direction and a layer of hydrogen atoms to passivate one side of the slab in order to suppress one of the two Au(111) surface states. 40 Å of vacuum was included in the simulation cell to

decouple the system from its periodic replicas in the direction perpendicular to the surface. Calculations were done within the AiiDA platform.[47]

ASSOCIATED CONTENT

Supporting Information

The Supporting Information is available free of charge on the ACS Publications website.
Procedures of experimental details and data and theoretical calculations (PDF)

AUTHOR INFORMATION

Corresponding Author

*Dr. José I. Urgel: jose-ignacio.urgel@empa.ch
*Prof. Roman Fasel: roman.fasel@empa.ch
*Prof. Kenichiro Itami: itami@chem.nagoya-u.ac.jp

ORCID

José I. Urgel: 0000-0001-7608-2979
Marco Di Giovannantonio: 0000-0001-8658-9183
Roman Fasel: 0000-0002-1553-6487
Yasutomo Segawa: 0000-0001-6439-8546
Lawrence Scott: 0000-0003-3496-8506
Kenichiro Itami: 0000-0001-5227-7894
Pascal Ruffieux: 0000-0001-5729-5354

Notes

The authors declare no competing financial interests.

ACKNOWLEDGMENT

This work was supported by the Swiss National Science Foundation, the European Union's Horizon 2020 research and innovation programme (GrapheneCore2 785219), the Office of Naval Research (N00014-18-1-2708), the ERATO program from JST (JPMJER1302 to K.I.), the Grant-in-aid for Scientific Research on Innovative Areas "π-Figuration" (JP17H05149 to Y.S.), and the U.S. National Science Foundation (CHE-1149096). The Swiss National Supercomputing Centre (CSCS) under project ID s746 and s904 are acknowledged for computational resources. The Swiss National Centre for Computational Design and Discovery of Novel Materials (MARVEL) is acknowledged for financial support. We thank Shantanu Mishra and Karl-Heinz Ernst for fruitful scientific discussions.

REFERENCES

(1) Novoselov, K. S.; Geim, A. K.; Morozov, S. V.; Jiang, D.; Zhang, Y.; Dubonos, S. V.; Grigorieva, I. V.; Firsov, A. A. Electric Field Effect in Atomically Thin Carbon Films. *Science* **2004**, *306*, 666–669.

(2) Segawa, Y.; Ito, H.; Itami, K. Structurally Uniform and Atomically Precise Carbon Nanostructures. *Nat. Rev. Mater.* **2016**, *1*.

(3) Novoselov, K. S.; Fal′ko, V. I.; Colombo, L.; Gellert, P. R.; Schwab, M. G.; Kim, K. A Roadmap for Graphene. *Nature* **2012**, *490*, 192–200.

(4) Schwierz, F. Graphene Transistors. *Nat. Nanotechnol.* **2010**, *5*, 487–496.

(5) Saito, M.; Shinokubo, H.; Sakurai, H. Figuration of Bowl-Shaped π-Conjugated Molecules: Properties and Functions. *Mater. Chem. Front.* **2018**, *2*, 635–661.

(6) Sgobba, V.; M. Guldi, D. Carbon Nanotubes —Electronic/Electrochemical Properties and Application for Nanoelectronics and Photonics. *Chem. Soc. Rev.* **2009**, *38*, 165–184.

(7) Kroto, H. W.; Heath, J. R.; O'Brien, S. C.; Curl, R. F.; Smalley, R. E. C60: Buckminsterfullerene. *Nature* **1985**, *318*, 162–163.

(8) Iijima, S. Helical Microtubules of Graphitic Carbon. *Nature* **1991**, *354*, 56–58.

(9) Cai, J.; Ruffieux, P.; Jaafar, R.; Bieri, M.; Braun, T.; Blankenburg, S.; Muoth, M.; Seitsonen, A. P.; Saleh, M.; Feng, X.; Müllen, K.; Fasel, R. Atomically Precise Bottom-up Fabrication of Graphene Nanoribbons. *Nature* **2010**, *466*, 470–473.

(10) Mackay, A. L.; Terrones, H. Diamond from Graphite. *Nature* **1991** ,*352*, 762.

(11) Ōsawa, E.; Yoshida, M.; Fujita, M. Shape and Fantasy of Fullerenes. *MRS Bull.* **1994**, *19*, 33–36.

(12) Townsend, S. J.; Lenosky, T. J.; Muller, D. A.; Nichols, C. S.; Elser, V. Structural Models of Negatively Curved Graphitic Carbon. *MRS Online Proc. Libr. Arch.* **1992**, *270*.

(13) Tagami, M.; Liang, Y.; Naito, H.; Kawazoe, Y.; Kotani, M. Negatively Curved Cubic Carbon Crystals with Octahedral Symmetry. *Carbon* **2014**, *76*, 266–274.

(14) Cheung, K. Y.; Xu, X.; Miao, Q. Aromatic Saddles Containing Two Heptagons. *J. Am. Chem. Soc.* **2015**, *137*, 3910–3914.

(15) Yamamoto, K.; Harada, T.; Nakazaki, M.; Naka, T.; Kai, Y.; Harada, S.; Kasai, N. Synthesis and Characterization of [7]Circulene. *J. Am. Chem. Soc.* **1983**, *105*, 7171–7172.

(16) Yamamoto, K.; Saitho, Y.; Iwaki, D.; Ooka, T. [7.7]Circulene, a Molecule Shaped Like a Figure of Eight. *Angew. Chem. Int. Ed. Engl.* **1991**, *30*, 1173–1174.

(17) Feng, C.-N.; Kuo, M.-Y.; Wu, Y.-T. Synthesis, Structural Analysis, and Properties of [8]Circulenes. *Angew. Chem.* **2013**, *125*, 7945–7948.

(18) Miller, R. W.; Duncan, A. K.; Schneebeli, S. T.; Gray, D. L.; Whalley, A. C. Synthesis and Structural Data of Tetrabenzo[8]Circulene. *Chem. – Eur. J.* **2014**, *20*, 3705–3711.

(19) Kawasumi, K.; Zhang, Q.; Segawa, Y.; Scott, L. T.; Itami, K. A Grossly Warped Nanographene and the Consequences of Multiple Odd-Membered-Ring Defects. *Nat. Chem.* **2013**, *5*, 739–744.

(20) Lin, H.-A.; Sato, Y.; Segawa, Y.; Nishihara, T.; Sugimoto, N.; Scott, L. T.; Higashiyama, T.; Itami, K. A Water-Soluble Warped Nanographene: Synthesis and Applications for Photoinduced Cell Death. *Angew. Chem. Int. Ed.* **2018**, *57*, 2874–2878.

(21) Jameh-Bozorghi, S.; Soleymanabadi, H. Warped C80H30 Nanographene as a Chemical Sensor for CO Gas: DFT Studies. *Phys. Lett. A* **2017**, *381*, 646–651.

(22) Dai, Y.; Li, Z.; Yang, J. Distinct Molecule Adsorption Behaviors on Warped Nanographene C80H30: A Theoretical Study. *Carbon* **2016**, *100*, 428–434.

(23) Wang, X.; Yu, S.; Lou, Z.; Zeng, Q.; Yang, M. Optical Absorption of Warped Nanographenes Tuned by Five- and Seven-Membered Carbon Rings. *Phys. Chem. Chem. Phys.* **2015**, *17*, 17864–17871.
(24) Scanning Tunneling Microscopy - 1st Edition https://www.elsevier.com/books/scanning-tunneling-microscopy/lucatorto/978-0-12-674050-9 (accessed Nov 12, 2018).
(25) Ernst, K.-H. Molecular Chirality at Surfaces. *Phys. Status Solidi B* **2012**, *249*, 2057–2088.
(26) Gross, L.; Mohn, F.; Moll, N.; Liljeroth, P.; Meyer, G. The Chemical Structure of a Molecule Resolved by Atomic Force Microscopy. *Science* **2009**, *325*, 1110–1114.
(27) Urgel, J. I.; Hayashi, H.; Di Giovannantonio, M.; Pignedoli, C. A.; Mishra, S.; Deniz, O.; Yamashita, M.; Dienel, T.; Ruffieux, P.; Yamada, H.; Fasel, R. On-Surface Synthesis of Heptacene Organometallic Complexes. *J. Am. Chem. Soc.* **2017**, *139*, 11658–11661.
(28) Krüger, J.; García, F.; Eisenhut, F.; Skidin, D.; Alonso, J. M.; Guitián, E.; Pérez, D.; Cuniberti, G.; Moresco, F.; Peña, D. Decacene: On-Surface Generation. *Angew. Chem.* **2017**, *129*, 12107–12110.
(29) Zuzak, R.; Dorel, R.; Kolmer, M.; Szymonski, M.; Godlewski, S.; Echavarren, A. M. Higher Acenes by On-Surface Dehydrogenation: From Heptacene to Undecacene. *Angew. Chem. Int. Ed.* **2018**, *57*, 10500–10505.
(30) Urgel, J. I.; Mishra, S.; Hayashi, H.; Wilhelm, J.; Pignedoli, C. A.; Giovannantonio, M. D.; Widmer, R.; Yamashita, M.; Hieda, N.; Ruffieux, P.; Yamada, H.; Fasel, R. On-Surface Light-Induced Generation of Higher Acenes and Elucidation of Their Open-Shell Character. *Nat. Commun.* **2019**, *10*, 861.
(31) Wagner, C.; Kasemann, D.; Golnik, C.; Forker, R.; Esslinger, M.; Müllen, K.; Fritz, T. Repulsion between Molecules on a Metal: Monolayers and Submonolayers of Hexa-Peri-Hexabenzocoronene on Au(111). *Phys. Rev. B* **2010**, *81*, 035423.
(32) Huempfner, T.; Sojka, F.; Forker, R.; Fritz, T. Growth of Coronene on (100)- and (111)-Surfaces of Fcc-Crystals. *Surf. Sci.* **2015**, *639*, 80–88.
(33) Gyarfas, B. J.; Wiggins, B.; Zosel, M.; Hipps, K. W. Supramolecular Structures of Coronene and Alkane Acids at the Au(111)−Solution Interface: A Scanning Tunneling Microscopy Study. *Langmuir* **2005**, *21*, 919–923.
(34) Anh Pham, T.; Song, F.; Nguyen, M.-T.; Stöhr, M. Self-Assembly of Pyrene Derivatives on Au(111): Substituent Effects on Intermolecular Interactions. *Chem. Commun.* **2014**, *50* (91), 14089–14092. https://doi.org/10.1039/C4CC02753A.
(35) Figueira-Duarte, T. M.; Müllen, K. Pyrene-Based Materials for Organic Electronics. *Chem. Rev.* **2011**, *111*, 7260–7314.
(36) Schull, G.; Berndt, R. Orientationally Ordered (7 × 7) Superstructure of C 60 on Au(111). *Phys. Rev. Lett.* **2007**, *99*.
(37) Bauert, T.; K. Baldridge, K.; S. Siegel, J.; Ernst, K.-H. Surface-Assisted Bowl-in-Bowl Stacking of Nonplanar Aromatic Hydrocarbons. *Chem. Commun.* **2011**, *47*, 7995–7997.
(38) Stöckl, Q. S.; Hsieh, Y.-C.; Mairena, A.; Wu, Y.-T.; Ernst, K.-H. Aggregation of C70-Fragment Buckybowls on Surfaces: π–H and π–π Bonding in Bowl Up-Side-Down Ensembles. *J. Am. Chem. Soc.* **2016**, *138*, 6111–6114.
(39) Mishra, S.; Krzeszewski, M.; Pignedoli, C. A.; Ruffieux, P.; Fasel, R.; Gryko, D. T. On-Surface Synthesis of a Nitrogen-Embedded Buckybowl with Inverse Stone–Thrower–Wales Topology. *Nat. Commun.* **2018**, *9*, 1714.
(40) Xu, K.; Urgel, J. I.; Eimre, K.; Di Giovannantonio, M.; Keerthi, A.; Komber, H.; Wang, S.; Narita, A.; Berger, R.; Ruffieux, P.; Pignedoli, C. A.; Liu, J.; Müllen, K.; Fasel, R.;

Feng, X. On-Surface Synthesis of a Nonplanar Porous Nanographene. *J. Am. Chem. Soc.* **2019**, *141*, 7726–7730.
(41) Wöll, C.; Chiang, S.; Wilson, R. J.; Lippel, P. H. Determination of Atom Positions at Stacking-Fault Dislocations on Au(111) by Scanning Tunneling Microscopy. *Phys. Rev. B* **1989**, *39*, 7988–7991.
(42) Gustafsson, A.; Okabayashi, N.; Peronio, A.; Giessibl, F. J.; Paulsson, M. Analysis of STM Images with Pure and CO-Functionalized Tips: A First-Principles and Experimental Study. *Phys. Rev. B* **2017**, *96*.
(43) Hammer, B.; Nørskov, J. K. Electronic Factors Determining the Reactivity of Metal Surfaces. *Surf. Sci.* **1995**, *343*, 211–220.
(44) Sinnokrot, M. O.; Valeev, E. F.; Sherrill, C. D. Estimates of the Ab Initio Limit for Π−π Interactions: The Benzene Dimer. *J. Am. Chem. Soc.* **2002**, *124*, 10887–10893.
(45) Xiao, W.; Ernst, K.-H.; Palotas, K.; Zhang, Y.; Bruyer, E.; Peng, L.; Greber, T.; Hofer, W. A.; Scott, L. T.; Fasel, R. Microscopic Origin of Chiral Shape Induction in Achiral Crystals. *Nat. Chem.* **2016**, *8*, 326–330.
(46) WSXM: A Software for Scanning Probe Microscopy and a Tool for Nanotechnology. *Rev. Sci. Instrum.* **2007**, *78*, 013705.
(47) Pizzi, G.; Cepellotti, A.; Sabatini, R.; Marzari, N.; Kozinsky, B. AiiDA: Automated Interactive Infrastructure and Database for Computational Science. Comput. Mater. Sci. 2016, 111, 218–230.